Biophysical Journal
Article

Biophysical Society

Mutation G1629E Increases von Willebrand Factor Cleavage via a Cooperative Destabilization Mechanism

Camilo Aponte-Santamaría,[1,2,*] Svenja Lippok,[3] Judith J. Mittag,[3] Tobias Obser,[4] Reinhard Schneppenheim,[4] Carsten Baldauf,[5] Frauke Gräter,[1,2] Ulrich Budde,[6] and Joachim O. Rädler[3]

[1]Molecular Biomechanics Group, Heidelberg Institute for Theoretical Studies, Heidelberg, Germany; [2]Interdisciplinary Center for Scientific Computing, Heidelberg University, Heidelberg, Germany; [3]Faculty of Physics and Center for NanoScience, Ludwig Maximilian University, Munich, Germany; [4]Department of Pediatric Hematology and Oncology, University Medical Center Hamburg-Eppendorf, Hamburg, Germany; [5]Theory Department, Fritz-Haber-Institut der Max-Planck-Gesellschaft, Berlin, Germany; and [6]Medilys Coagulation Laboratory, Asklepios Klinic Altona, Hamburg, Germany

ABSTRACT The large multimeric glycoprotein von Willebrand Factor (VWF) plays a pivotal adhesive role during primary hemostasis. VWF is cleaved by the protease ADAMTS13 as a down-regulatory mechanism to prevent excessive VWF-mediated platelet aggregation. For each VWF monomer, the ADAMTS13 cleavage site is located deeply buried inside the VWF A2 domain. External forces in vivo or denaturants in vitro trigger the unfolding of this domain, thereby leaving the cleavage site solvent-exposed and ready for cleavage. Mutations in the VWF A2 domain, facilitating the cleavage process, cause a distinct form of von Willebrand disease (VWD), VWD type 2A. In particular, the VWD type 2A Gly1629Glu mutation drastically accelerates the proteolytic cleavage activity, even in the absence of forces or denaturants. However, the effect of this mutation has not yet been quantified, in terms of kinetics or thermodynamics, nor has the underlying molecular mechanism been revealed. In this study, we addressed these questions by using fluorescence correlation spectroscopy, molecular dynamics simulations, and free energy calculations. The measured enzyme kinetics revealed a 20-fold increase in the cleavage rate for the Gly1629Glu mutant compared with the wild-type VWF. Cleavage was found cooperative with a cooperativity coefficient $n = 2.3$, suggesting that the mutant VWF gives access to multiple cleavage sites of the VWF multimer at the same time. According to our simulations and free energy calculations, the Gly1629Glu mutation causes structural perturbation in the A2 domain and thereby destabilizes the domain by ~10 kJ/mol, promoting its unfolding. Taken together, the enhanced proteolytic activity of Gly1629Glu can be readily explained by an increased availability of the ADAMTS13 cleavage site through A2-domain-fold thermodynamic destabilization. Our study puts forward the Gly1629Glu mutant as a very efficient enzyme substrate for ADAMTS13 activity assays.

INTRODUCTION

The multimeric protein von Willebrand Factor (VWF) is essential for the initial platelet adhesion and subsequent thrombus growth as it promotes the binding of platelets to injured vessel walls (1). The size distribution of VWF is regulated by the protease ADAMTS13 (a disintegrin and metalloprotease with thrombospondin type 1 motif, member 13). The enzymatic cleavage of VWF by ADAMTS13 represents a crucial control mechanism in hemostasis (2,3). The ADAMTS13 specific cleavage site of VWF is located at the peptide bond Tyr1605-Met1606, which is deeply buried in the VWF A2 domain (4) (Fig. 1, *A* and *B*). This has been shown to be mechanosensitive such that the A2 cleavage site is accessible only if the A2 domain is mechanically stretched (5–7). We recently showed that shear flow in vitro, above a critical shear rate, results in ADAMTS13 specific cleavage of full-length VWF, in agreement with hydrodynamic models of flow-induced shear stress in VWF multimers (8). In vivo, stretching is believed to be triggered by shear flow, for instance arising at injured endothelium or stenosed arteries.

A severely deficient ADAMTS13 activity correlates with increased amounts of highly active, high molecular weight multimers (HMWM) of VWF that cause a thrombotic microangiopathy, which is commonly referred to as thrombotic thrombocytopenic purpura (TTP) (9–11). TTP is caused

Submitted July 21, 2016, and accepted for publication November 30, 2016.

*Correspondence: camilo.aponte@h-its.org

Camilo Aponte-Santamaría and Svenja Lippok contributed equally to this work.

Editor: Elizabeth Rhoades

http://dx.doi.org/10.1016/j.bpj.2016.11.3202

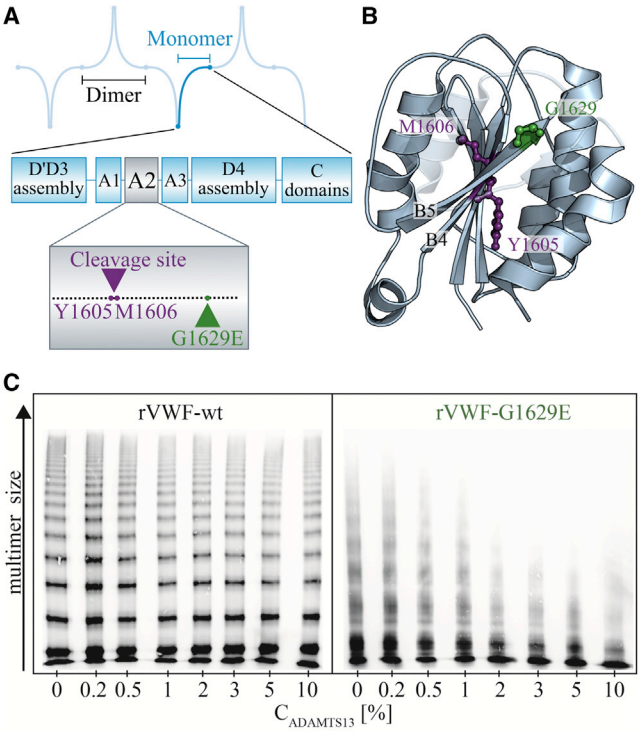

FIGURE 1 ADAMTS13-dependent proteolysis of VWF. (*A*) The scheme depicts a VWF multimer indicating the domains which constitute a VWF monomer and highlighting the ADAMTS13 Y1605-M1606 cleavage site in the A2 domain (*purple*). The von Willebrand factor disease type 2A mutation G1629E increases ADAMTS13-mediated VWF proteolysis (*green*). (*B*) Secondary structure of the A2 domain (*cartoon*) is shown. The cleavage-site residues Y1605 and M1606 are buried at the core of the protein in the beta strand B4 (*purple sticks and balls*). The G1629 residue locates in the strand B5 (*green sticks and spheres*). Flow induces the unfolding of the A2 domain, thereby exposing the cleavage site to ADAMTS13. (*C*) Multimer analysis of ADAMTS13-induced cleavage is provided. ADAMTS13 concentration represented in percentage of normal plasma level. In nondenaturing buffer, wild-type recombinant VWF (rVWF-wt) showed no degradation up to ADAMTS13 concentrations of 10% (*left panel*). The mutant rVWF-G1629E shows the characteristic bands of degrading VWF multimers with increasing ADAMTS13 concentrations (*right panel*). To see this figure in color, go online.

either by mutations of the ADAMTS13 gene or by acquired autoantibodies that inhibit ADAMTS13 activity (12). In contrast, quantitatively and/or functionally deficient VWF causes the common bleeding disorder von Willebrand disease (VWD) (13,14). There are several mutations in the VWF A2 domain, identified in patients with VWD, which induce increased ADAMTS13-mediated proteolysis of VWF (13,14). This pathological condition is known as VWD type 2A with enhanced proteolysis, featuring a profound deficiency of the functionally most active VWF-HMWM.

Enhanced proteolysis has been attributed to mutation-induced structural destabilization of the A2 domain, which promotes its unfolding and thereby facilitates exposure of the ADAMTS13 cleavage site (7,15,16). In a broad study, Hassenpflug et al. investigated the impact of 13 different clinically relevant VWD type 2A mutations on ADAMTS13-dependent proteolysis (17). They found that 11 of the studied mutants showed increased specific proteolysis compared with wild-type VWF. For four of these mutants (Gly1609Arg, Ile1628Thr, Gly1629Glu, and Gly1631Asp), this even held true in the absence of denaturing urea. Intriguingly, these four mutants, when expressed by recombinant techniques, featured normal protein expression and normal size distribution of VWF HMWM. Moreover, the three mutations in which a glycine residue was replaced by a charged residue (Gly1609Arg, Gly1629Glu, and Gly1631Asp) exhibited both an increased proteolysis of full-length multimers and of VWFA1-A2-A3 fragments. The latter constitutes a simple system to monitor the specific action of ADAMTS13 on VWF, and it is thereby of potential use for the detection of ADAMTS13 in vitro. In particular, the mutant Gly1629Glu displayed the most dramatic acceleration in ADAMTS13-mediated proteolysis, even under nondenaturing conditions. Therefore it constitutes a very promising candidate to develop highly sensitive diagnostic ADAMTS13-detection assays.

Although the effect of the Gly1629Glu (G1629E) mutation on the static multimer size distribution has been determined (17), quantification of its impact on the cleavage kinetics is lacking so far. Furthermore, the molecular mechanism by which this mutation drastically enhances proteolytic cleavage remains to be fully resolved. In this study, we address these issues by using fluorescence correlation spectroscopy (FCS), molecular dynamics (MD) simulations, and free energy calculations. We used FCS, in addition to VWF multimer analysis, to detect in vitro the cleavage of full-length recombinant G1629E mutant VWF (rVWF-G1629E) compared with recombinant wild-type VWF (rVWF-wt). We observed an increment of the cleavage rate for the rVWF-G1629E mutant to timescales of minutes, in the absence of mechanical stress or denaturing agents. This was found to be ~20-fold faster than the cleavage rate for denatured rVWF-wt. The enzyme kinetics exhibited cooperative behavior with a cooperativity coefficient $n = 2.3$ in contrast to non-cooperative Michaelis-Menten type kinetics found for native VWF under denaturant conditions (8). Free energy calculations and MD simulations support the hypothesis that the elevated propensity of VWF-G1629E to ADAMTS13 cleavage is due to the destabilization of the mutated A2 domain. We discuss possible applications of rVWF-G1629E as enzyme substrate for standard ADAMTS13 assays in clinical laboratories.

MATERIALS AND METHODS

Protein expression

Recombinant fusion proteins of green fluorescence protein (eGFP) with rVWF-wt and rVWF-G1629E, respectively, were produced as described before (18). rVWF-wt and rVWF-G1629E proteins were expressed as multimers, whereby each monomer was linked to an eGFP protein at the

C-terminal domain. Full-length ADAMTS13 cDNA was cloned into the expression vector pIRES neo2 for stable transfection of HEK 293 cells by liposomal transfer under selective pressure 48 h after transfection (17). Wild-type rhuADAMTS13, secreted to the medium, was used for cleavage experiments.

Plasma samples

Plasma samples were collected from normal volunteer donors in S-monovettes, coagulation sodium citrate (Sarstedt, Germany). After leaving the sample at room temperature for 30 min, they were centrifuged (10 min, 2300 rpm). The supernatant was stored at –80°C until further use. Informed consent was obtained from all subjects.

Multimer analysis

rVWF-G1629E (1 U/mL) with a full spectrum of multimers was first dialyzed in 5 mM Tris-HCl (pH 8.0) and thereafter mixed with plasma samples (containing normal concentrations of ADAMTS13) diluted in 5 mM TriHCl (pH 8.0). After activation with 250 mM BaCl2 ADAMTS13-mediated cleavage took place for 3 h at 37°C. VWF multimer analysis was carried out by sodium dodecyl sulfate (SDS) agarose gel electrophoresis, immuno blotting, and luminescent visualization as described in (19). The luminescent blot was saved on electronic media via photo imaging (FluorChem8000; Alpha Innotech, San Leandro, CA) (20).

FCS

Purified rVWF-G1629E fusioned to eGFP was added to blood plasma and the fluorescence intensity in a laser focus was monitored over time. The autocorrelation of the fluorescence signal determined the number concentration of fluorescent VWF molecules online. This was achieved by means of the amplitude of the autocorrelation curve $G(0)$, which is inversely proportional to the number of fluorescent molecules in the confocal volume, $G(0) \sim 1/N$ (21). Thus, cleavage of fluorescent rVWF-G1629E multimers by ADAMTS13 is detected by the increase of the effective number of fluorescent VWF molecules. FCS measurements were run on an Axiovert 200 microscope with a ConfoCor 2 unit (Carl Zeiss, Jena, Germany), equipped with a 40× (NA = 1.2) water-immersion Apochromat objective (Carl Zeiss) and a 488 nm argon laser for illumination. Experiments were carried out in eight-well LabTek I chamber slides (Nunc, Rochester, NY) in 5 mM Tris-HCl (pH 8.0) containing 10 mM BaCl2 for 10 times 6 min on rVWF-G1629E and for 20 times 9 min on rVWF-wt (owing to the decreased cleavage). For measurements in blood plasma, the plasma was diluted to the desired concentration with Tris-HCl buffer. For rVWF-wt, 1.5 M urea was added, based on the commonly used protocol (2,22,23). The setup was calibrated measuring eGFP for 20 times 60 s in the corresponding buffer. The temperature was set to 37°C (heating stage, ibidi GmbH, Martinsried, Germany). Correlation analysis was performed using the ConfoCor 2 software. FCS data was analyzed as described in detail before (8). Analysis of diffusion constants for recombinant VWF constructs recovered from FCS is presented in the Supporting Material. FCS measurements under blood plasma conditions was performed by adding recombinant rVWF-G1629E to varying concentrations of normal plasma of a healthy volunteer. In this case, ADAMTS13 activity was quantified in highly diluted plasma samples, containing only 1% to 5% normal plasma (NP).

Free energy calculations

Free energy calculations were performed to determine whether the G1629E mutation destabilizes the VWF A2 domain. The relevant measure for this destabilization is the difference in unfolding free energies for the mutant and the wild-type protein: $\Delta F_{G1629E} - \Delta F_{wt}$. This quantity was computed following the thermodynamic cycle, from the free energy difference due to the mutation in the folded (ΔF_1) and unfolded (ΔF_2) states, $\Delta F_2 - \Delta F_1$. ΔF_1 and ΔF_2 were obtained by performing multiple nonequilibrium MD runs, in which the glycine residue was mutated into a glutamic acid, and vice versa (see the Supporting Material). The free energy was estimated via the Crooks fluctuation theorem (24), from the nonequilibrium work associated to this transition, by means of a Bennett acceptance ratio as maximum likelihood estimator, a method proposed by Shirts et al. (25) to estimate equilibrium free energies from nonequilibrium measurements (a method called here BAR-ML). For comparison, we also predicted a rough estimate of the free energy by computing the intercept of the work distributions recovered from forward (glycine to glutamic acid) and backward (glutamic acid to glycine) nonequilibrium transitions (26,27) (an approach named here Intercept). See details of the free energy calculations in the Supporting Material. The corresponding change in the equilibrium unfolding constant upon mutation was estimated from $\exp[-(\Delta F_{G1629E} - \Delta F_{wt})/k_BT]$, with k_B the Boltzmann constant and T the temperature. In our case, T was 300 K, therefore k_BT was approximately 2.5 kJ/mol.

Equilibrium MD simulations

Equilibrium MD simulations were carried out starting from the solvated conformation of the VWF A2 domain (x-ray structure PDB: 3GXB (15)). Simulations were performed with the GROMACS package (28–30) (4.5.5 version) following the procedure described in (31), both for the wild-type domain (five runs of 200 ns each for 1 μs concatenated simulated time, one of the runs taken from our previous study (31)) and for the mutant G1629E (four runs of 200 ns each for 0.8 μs concatenated simulated time). The first 50 ns of the simulations were considered as equilibration time and discarded for further analysis. The G1629E mutation was introduced by using the PyMOL software (32). See details in the Supporting Material.

A partial least square functional mode analysis (PLS-FMA), consisting of a multivariate linear regression (33), was carried out to identify conformational changes of the VWF A2 domain induced by the mutation G1629E (see details in the Supporting Material). The root mean square fluctuation (RMSF) of the atomic positions was computed by time-averaging concatenated simulations of either the wild-type or the mutant domain. Force distribution analysis (FDA) (34) was performed to monitor changes in the internal stress of the protein upon mutation. Time-averaged pairwise forces $\langle F_{ij} \rangle$ were computed for all residue pairs (i,j) of the A2 domain, in its wild-type ($\langle F_{ij}(\text{wt}) \rangle$) and mutated ($\langle F_{ij}(\text{G1629E}) \rangle$) forms. The difference $\Delta F_{ij} = \langle F_{ij}(\text{G1629E}) \rangle - \langle F_{ij}(\text{wt}) \rangle$ was subsequently calculated as a measure of the change in internal stress after mutation.

RESULTS

Multimer analysis

We first corroborated the increased degradation of VWF containing the G1629E mutation, under nondenaturing conditions, using gel analysis (Fig. 1 *C*). Different ADAMTS13 concentrations were added to a constant amount of rVWF-wt and rVWF-G1629E, respectively. Whereas no shift in multimer sizes was detected for rVWF-wt up to ADAMTS13 concentrations of 10% of the physiological amount in normal plasma, NP (Fig. 1 *C*, *left*), multimer sizes decreased rapidly for rVWF-G1629E with increasing ADAMTS13 concentration (Fig. 1 *C*, *right*). Note, that even in the absence of ADAMTS13 the VWF mutant was degraded to some extent just after dialysis in the 5 mM Tris-HCl. Hence, our recombinant proteins (wild-type and

mutated) reproduced the same cleavage response as in previous studies (17).

Fluorescence in vitro assay to monitor ADAMTS-13 mediated cleavage

We next devised an in vitro FCS assay to go beyond static gel assays and thereby monitor over time the cleavage of rVWF-G1629E by ADAMTS13. Fig. 2 *A* illustrates the FCS autocorrelation signal of 6 nM rVWF-G1629E at four successive time points, in the presence of ADAMTS13 at a concentration of 0.3 U/mL (30% NP). The amplitude of the autocorrelation shifted toward lower values, thus indicating that fluorescent rVWF-G1629E multimers are cleaved by ADAMTS13. Note that neither denaturing substances nor shear flow were applied for these experiments. Nevertheless, cleavage was observed within minutes (Fig. 2 *A*, *inset*). The increment of rVWF-G1629E fluorescent fragments, and thereby of the protein concentration, with time defines the cleavage rate *dC/dt* (expressed in molar VWF concentration over time in Fig. 2 *A*, *inset*). Therefore, our FCS assay directly quantifies the VWF cleavage rate—without denaturants or flow—and thereby can be used as a measure for ADAMTS13 activity.

Cleavage kinetics of rVWF-G1629E

We quantified the ADAMTS13-mediated cleavage kinetics of rVWF-G1629E by using FCS (Fig. 2 *B*). We find a positive *reinforcing* effect similar to a cooperative Hill-type behavior, i.e., the probability of binding to a cleavage site of one multimer is enhanced immediately after cleaving the same multimer at another site. Fitting with $dC/dt = v_{max}/(1 + (K_A/C)^n)$ yields a cooperativity coefficient $n = 2.3 \pm 0.2$, a maximum cleavage rate $v_{max} = 143.2 \pm 0.4$ pM/min, and a VWF-G1629E concentration producing half maximum cleavage $K_A = 11.5 \pm 0.5$ nM. In the case of more dilute plasma (0.17% NP), we obtained $n = 2.4 \pm 1.3$, $v_{max} = 74.1 \pm 7$ pM/min, $K_A = 11.9 \pm 2$ nM consistent with the 0.5% NP data. Note that for cleavage of the denatured VWF-wt, we previously observed noncooperative Michaelis-Menten kinetics (8). Moreover, a 15-fold-reduced Michaelis-Menten constant $K_M = 171 \pm 85$ nM was found compared with the K_A value for rVWF-G1629E cleavage.

We next investigated the effect of increasing the concentration of ADAMTS13 in the buffer on the cleavage rate of rVWF-G1629E (Fig. 2 *C*). We considered a physiologically and clinically relevant range of ADAMTS13 concentrations, ranging from 5% to 30% of the NP amount. rVWF-G1629E concentration was maintained constant at 6 nM, within the most sensitive concentration regime for FCS measurements. Within that range, we detected a linear response, whose fit yielded an increase of the cleavage rate of 1.61 ± 0.08 nM/min/$[C_{ADAMTS13}]$ (with $[C_{ADAMTS13}]$ the ADAMTS13 concentration in % of NP). Note that a similar linear response increment (1.50 ± 0.04 nM/min/$[C_{ADAMTS13}]$) was obtained when reducing the concentration range down to 0.5% to 5% (inset of Fig. 2 *C*). This demonstrates that the FCS assay is highly sensitive for rVWF-G1629E cleavage by ADAMTS13 at activities down to 0.5% of the physiological level. This feature could be exploited to improve the detection resolution of commonly used diagnostic assays, which lies between 2.5% and 5% (35,36).

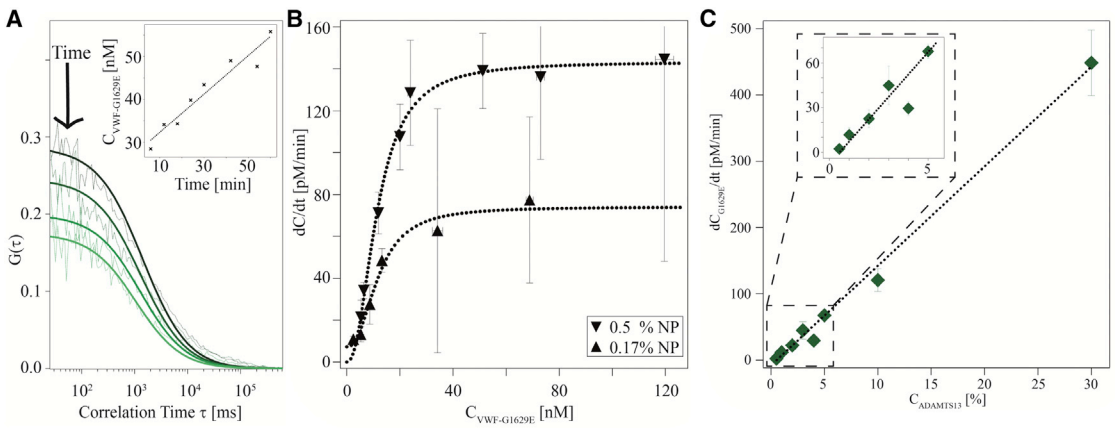

FIGURE 2 Cleavage kinetics of rVWF-G1629E measured by FCS. (*A*) Autocorrelation curve $G(\tau)$ is shown. The amplitude at $\tau = 0$, $G(\tau = 0)$, is inversely proportional to the number of fluorescent molecules N in the detection volume. N increases with time due to cleavage of the VWF multimers. Inset: the increase in particle concentration is plotted over time. The slope of the curve defines the cleavage rate *dC/dt*. (*B*) Cleavage kinetics of rVWF-G1629E in 0.17% and 0.5% NP is presented. The dashed lines indicate Hill-type activity with cooperativity coefficient $n = 2.4 \pm 1.3$ (0.17%) and $n = 2.3 \pm 0.2$ (0.5%), respectively. (*C*) Cleavage rate versus ADAMTS13 concentration is displayed. ADAMTS13 activity in buffer showing a linear increase with ADAMTS13 concentration represented in % of normal plasma level (0.3 U/mL corresponds to 30% NP). rVWF-G1629E concentration was held constant at 6 nM, within the most sensitive concentration regime for FCS measurements. Similar linear response is observed down to ADAMTS13 concentrations of 0.5%, as highlighted in the inset. Dotted lines correspond to linear fits to the measurements (*solid points*). To see this figure in color, go online.

Effect of the G1629E mutation on the cleavage kinetics

We measured the effect of the G1629E mutation on the proteolytic kinetics by comparing cleavage rages of the rVWF-G1629E mutant with those of rVWF-wt (Fig. 3). For rVWF-wt, a denaturing buffer was used to make the cleavage site accessible for ADAMTS13. Furthermore, threefold prolonged measurement times were needed to achieve a reliable signal-to-noise ratio. The urea-containing buffer could only partly unfold the A2 domains and not all of them, thereby not all the cleavage sites may have been fully exposed (37). FCS measurements of the diffusion coefficients of rVWF-wt dimer and rVWF-G1629E dimer in nondenaturing and denaturing buffer confirmed the observation of partial unfolding (Fig. S1). In contrast to this, for rVWF-G1629E, cleavage rates were increased 20-fold. Here, no denaturant was added, thus stressing on the remarkable protein destabilization imparted by the G1629E mutation. Consistently to the observed cooperative Hill-type behavior, the increase of protein concentration resulted in increased cleavage rates (compare 6 nM with 24 nM in Fig. 3). Taken together, our FCS results show that the G1629E mutation has a profound effect not only on the (static) VWF size distribution upon cleavage, but also on the actual kinetics of this process.

Free energy calculations

Our experiments raised the question about the mechanism by which the G1629E mutation accelerates cleavage. The mutation could destabilize the VWF A2 domain, thereby making this domain more prone to unfold and to expose its Y1605-M1606 cleavage site faster in its mutated form compared with its wild-type form. The structural consequences of other VWD type 2A mutations on the integrity of the A2 domain have been assessed in earlier MD simulations (16). For direct comparison with the FCS measurements, we quantified the extent of destabilization by performing MD-based free energy calculations (Fig. 4). We assessed the thermodynamic stability of the A2 domain upon G1629E mutation from the difference in unfolding free energies of the wild-type (ΔF_{wt}) and the mutant (ΔF_{G1629E}), which we computed following the thermodynamic cycle depicted in Fig. 4. We obtained $\Delta F_{G1629E} - \Delta F_{wt} = -11.8(2.4)$ kJ/mol using the BAR-ML method. This value is consistent with the rough estimate of $-9(<6)$ kJ/mol, derived with the Intercept approach (Fig. S2) and with the value of –8.4 kJ/mol obtained from the PoPMuSIC web server (38), an estimate based on the static x-ray structure of the A2 domain. The predicted value (–11.8 kJ/mol) is fivefold larger than its statistical error (2.4 kJ/mol), thus $\Delta F_{G1629E} - \Delta F_{wt}$ is significantly smaller than zero. Gapsys et al. (39), in a recent large-scale scan mutation study, demonstrated that charged-changing mutations (as it is our case) induce free-energy changes deviating around 4.32 kJ/mol from the experimental values. Although this study was conducted for a different protein, it suggest that if we underestimated the free energy difference, it would not be by more than 4.32 kJ/mol, supporting therefore that our predictions (–9 or –11.8 kJ/mol) are significantly distant from 0. A negative value of $\Delta F_{G1629E} - \Delta F_{wt}$ implies that unfolding is energetically more favorable for the mutant. Thus, the G1629E mutation thermodynamically destabilizes the A2 domain.

The computed free energy difference results in a ~110 fold increase in the equilibrium unfolding constant of the

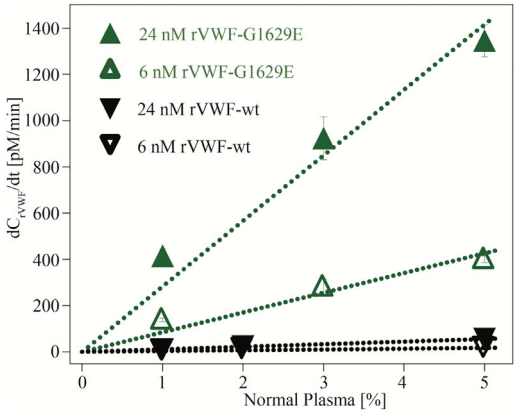

FIGURE 3 Cleavage of the mutant rVWF-G1629E compared with cleavage of rVWF-wt both in normal plasma (1.5 M of urea was added in the case of rVWF-wt as a denaturing agent). The cleavage of mutant rVWF-G1629E is increased 20-fold compared with denatured rVWF-wt. Linear fits are indicated as dotted lines. Highly diluted plasma samples, containing only 1% to 5% of normal plasma, were considered. To see this figure in color, go online.

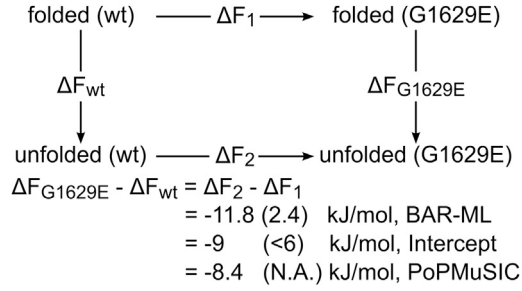

FIGURE 4 Free energy calculations reveal a destabilization of the VWF A2 domain upon G1629E mutation. The thermodynamic cycle depicts the change in protein stability of the A2 domain upon the G1629E mutation. We computed the difference in free energy, $\Delta F_{G1629E} - \Delta F_{wt}$, by using the Bennett acceptance ratio as a maximum-likelihood estimator (called here BAR-ML), a method to estimate equilibrium free energies from nonequilibrium calculations (25). For comparison, we also predicted rough estimates of the free energy by computing the intercept of nonequilibrium forward and backward work distributions (called here Intercept) and by using the PoPMuSIC web server (38) that yields an estimate based on the static x-ray structure of the A2 domain. We obtained $\Delta F_{G1629E} < \Delta F_{wt}$ implying a destabilization and shorter unfolding time for the mutated A2 domain. Values in parenthesis indicate the error estimate, which is an upper boundary in the case of the Intercept method.

VWF A2 domain upon mutation employing BAR-ML (~30- to 40-fold using the PoPMuSIC and the Intercept rough methods, respectively). This increase in rate is in qualitative agreement with our cleavage measurements in the absence of urea and shear, which showed no cleavage of the VWF-wt, even after waiting 3 to 5 h, and a substantial reduction of this dwell time to ~15 min for the VWF-G1629E mutant. Our calculations thus suggest that increased ADAMTS13 cleavage rates are attributable to a local destabilization causing faster unfolding of the mutated VWF A2 domain.

Molecular dynamics simulations of the VWF A2 domain with and without G1629E mutation

We performed equilibrium MD simulations to examine the structural destabilization of A2 induced by the G1629E mutation, which gives rise to the increased cleavage rates (Fig. 5). Within the simulated timescale of hundreds of nanoseconds, the A2 domain remained folded in both its wild-type and its mutant form, maintaining its globular shape and keeping the ADAMTS13 cleavage site Y1605-M1606 shielded. This suggests that stretching of the A2 domain, necessary for ADAMTS13 cleavage, occurs spontaneously on a longer timescale. Nevertheless, the simulations allowed us to capture sources of A2 destabilization. By using PLS-FMA, we identified primarily helix H5, located near the G1629 residue, as a region of major structural adaptations to the G1629E mutation, and, to a smaller extent, the loops L5-6 and L3-4, which are not in direct contact with the perturbed residue (Fig. 5 *A*). In accordance, we observed a broader conformational variability for the mutant due to statistically significant local fluctuations at the helix H5 and loop L5-6 (Fig. 5 *B*). Remarkably, the knotted C-terminal part of the protein (residue index < 1580) presented small RMSFs both for the wild-type and the mutant. This implies a high structural stability for this region and is in concordance with previous computational studies (7).

Finally, we analyzed whether the mechanical strength of the A2 domain was changed upon mutation. To this end, we computed the internal stress of the A2 domain in its wild-type and mutant forms. We observed that the mutation induced drastic changes in many of the residue pairwise forces, which provide a measure of the internal stress (Fig. 5 *C*). These changes were not only observed locally at the mutation site but also extended to other distant parts of the protein including the ones hiding the ADAMTS13 cleavage site. Thus, in addition to local structural changes adjacent to the site of mutation, the G1629E exchange also induces a global mechanical perturbation of the VWF A2 domain.

DISCUSSION

In this study, we quantified the impact of the VWD type 2A mutation G1629E on the cleavage kinetics of VWF, by using FCS. Furthermore, we provide a molecular explanation to the accelerated proteolysis imparted by this mutation, employing free energy calculations and MD simulations.

The FCS in vitro assay allowed us to go beyond conventional static gel analysis to obtain a kinetic description of the cleavage process. The fluorescence-based approach directly yielded the cleavage rate of VWF as a function of the ADAMTS13 concentration and revealed an acceleration of cleavage to timescales of minutes due to the G1629E mutation. The observed 20-fold increment in the cleavage rate for rVWF-1629E compared with rVWF-wt—even in the absence of denaturants or flow—implies that G1629E does not only modify the equilibrium size distribution, but it also strongly alters the cleavage kinetics of VWF. Previous gel analysis estimated ~5-fold increased cleavage rates for isolated A2 domains containing the VWD type 2A mutations I1628T and E1638K (16). Our study expands these findings by revealing G1629E as another mutation with increased proteolytic kinetic activity. Furthermore, our results suggest that FCS is a very flexible tool to assess the cleavage kinetics in principle of any construct all the way up to ultra-long VWF multimers, complementing single-domain standard gel assays.

The observed cooperative Hill-type cleavage behavior might possibly be attributable to the fact that the destabilized structure of several mutated A2 domains gives access to multiple cleavage sites at the same time. The hypothesis of a destabilized A2 domain in the mutant VWF is supported by MD simulations showing that the G1629E mutation induces structural and mechanical destabilization of this domain, near and well beyond the site of mutation. This result is consistent with previous MD simulations (16) that also identified structural perturbations of the A2 domain induced by other three VWD type 2A mutations. Destabilization was calculated to correspond to a free energy difference of ~11.8 kJ/mol using the BAR-ML method and of ~8–9 kJ/mol using either the Intercept method or the PoPMuSIC web server predictor. Note that determination of the free energy from the intercept of the forward and reverse work distributions suffers from the choice of the bin width of the distributions and the PoPMuSIC web server does not consider dynamic information. These difficulties are not encountered in the BAR-ML method. Hence, among the three, the BAR-ML estimate (–11.8 kJ/mol) constitutes the most accurate prediction of the change in free energy. This destabilization leads to a ~110-fold increase in VWF A2 unfolding probability in agreement with the experimental finding that cleavage by ADAMTS13 is strongly increased. Therefore, our computational approach did not only allow for the identification of structural perturbations of the A2 domain, induced by the G1629E mutation, but quantified the enhanced A2 unfolding probability, and thereby how readily it is prepared for cleavage. Beyond the scope of this article was to study other VWD type 2A mutations. Nevertheless, future studies could follow a

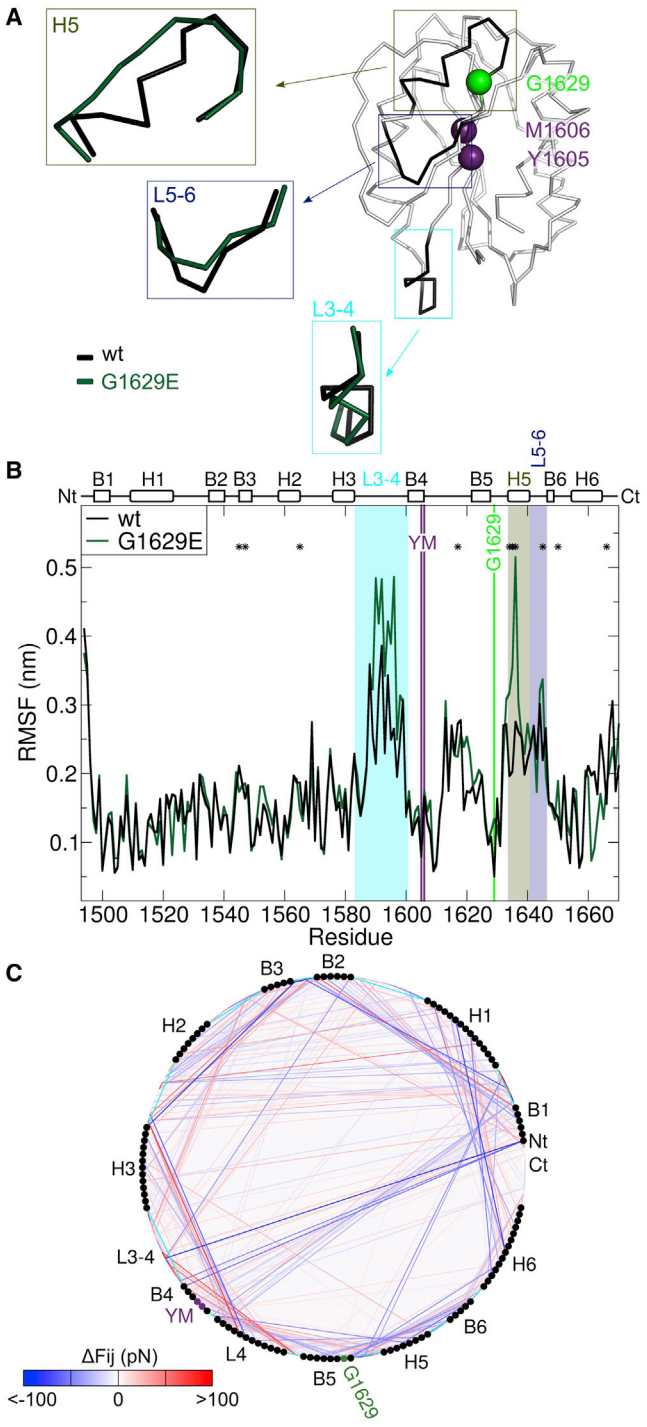

FIGURE 5 Structural, dynamic, and mechanical destabilization changes of the VWF A2 domain upon G1629E mutation recovered from MD simulations. (*A*) Structural changes of the A2 domain (*ribbon presentation*) induced by the G1629E mutation were recovered by performing a partial least square functional mode analysis on the MD simulations. Helix H5, and loops L5-6 and L3-4 showed the largest structural differences (*black*: wild-type, *green*: mutant). The alpha carbon atoms of the Y1605, M1606, and G1629 residues are presented with spheres. (*B*) RMSF of each residue is shown (same color code as in *A*). The secondary structure of the A2 domain (*top*) indicates the termini (Nt and Ct), the strands (B1...B6), the helices (H1...H6), and the loops (L3-4 and L5-6). The ADAMTS13 cleavage site Y1605-M1606 (YM) is highlighted in purple and G1629 in green. Residues with statistically significant differences in RMSF are highlighted with * (student's *t*-test, $p < 0.05$). Loop L3-4 showed pronounced but not statistically significant RMSF differences. (*C*) Changes in the internal stress of the protein upon G1629E mutation recovered by FDA are depicted. The secondary structure of the protein is spanned around the circle. Each point of the circle corresponds to a residue, ranging from the N-terminus at 0 degree to the C terminus at 360 degree. The Y1605-M1606 (YM) cleavage site and the G1629 residue are highlighted in color. Each line connecting two points corresponds to the difference ΔF_{ij} for the residue pair (i,j). Here, $\Delta F_{ij} = \langle F_{ij}(\text{G1629E})\rangle - \langle F_{ij}(\text{wt})\rangle$, with $\langle F_{ij}(\text{wt})\rangle$ the time-averaged pairwise force of the residue pair (i,j) in its wild-type form and $\langle F_{ij}(\text{G1629E})\rangle$ in its mutated form. ΔF_{ij} is displayed according to the color scale at the bottom, varying from a substantial reduction (*blue*) to a substantial increase (*red*) in the internal stress, with no change in white. Here, only statistically significant ΔF_{ij} are shown ($p < 0.05$). To see this figure in color, go online.

similar strategy, involving free energy calculations, to discern whether this group of mutations indeed destabilize the A2 domain. Interestingly, the three VWD type 2A mutations that featured normal protein expression and normal size distribution of VWF HMWM as well as an increased proteolysis of both full-length multimers and of VWFA1-A2-A3 fragments are replacements of a glycine residue by a charged residue (G1609R, G1629E, and G1631D). Furthermore, they locate in sequence not so far away from Glycine 1629. Therefore, it will be highly interesting to investigate whether these three mutations follow similar general destabilization principles as the one proposed here to induce accelerated proteolytic cleavage. Our approach could also be employed to test if the mutations may also enhance the binding of ADAMTS13 to the unfolded A2 domain, thus speeding up the recognition of the already-exposed cleavage site. This could be an alternative or additional molecular mechanism for VWD type 2A.

In summary, we studied the impact of the VWD type 2A mutation G1629E on the proteolytic cleavage of VWF driven by ADAMTS13. FCS measurements revealed that the loss of ultra-long multimers for the mutant VWF-1629E is associated to a dramatic cooperative increment in its proteolytic kinetic activity. To our knowledge, this constitutes the first quantification of the kinetic alteration of VWF cleavage due to a disease-related mutation. Free energy calculations and MD simulations support a molecular mechanism in which the increment in cleavage is associated with the destabilization of the VWF A2 domain. Such destabilization makes this domain more prone to unfold and thereby to expose more readily the ADAMTS13 cleavage site. FCS and MD-based free energy calculations offer an excellent combined approach to better understand VWD, by deciphering which mutations follow similar destabilizing mechanisms as G1629E and which ones on the contrary change the binding affinity of ADAMTS13 to A2.

The rVWF-G1629E mutant exhibited a linear response between the cleavage rate and the ADAMTS13 content, over a broad range of enzyme concentrations. In

consequence, rVWF-1629E could serve as a highly sensitive ADAMTS13 detection marker, even at very low enzyme concentrations (0% to 5% of the NP amount). This mutant also offers the advantage that it does not require denaturants or flow as catalyzing agents, as other commonly used assays employing rVWF or VWF fragments do. In consequence, rVWF-G1629E has potential use as a sensitive substrate for fast and accurate fluorescent-based laboratory tests of ADAMTS13 activity in full blood samples. Quantitative biophysical studies combined with molecular dynamics prove valuable to clarify specific enzymatic disease-related deficiencies of central constituents of the coagulation cascade, such as VWF, and potentially open opportunities for enhanced clinical diagnosis.

SUPPORTING MATERIAL

Supporting Material and Methods and three figures are available at http://www.biophysj.org/biophysj/supplemental/S0006-3495(16)34271-0.

AUTHOR CONTRIBUTIONS

J.O.R., C.A.-S., U.B., F.G., C.B., and R.S. designed the study. S.L. and J.J.M. performed the FCS experiments. C.A.-S. performed the free energy calculations and MD simulations. T.O. engineered the recombinant proteins. U.B. performed the multimer analysis. S.L., C.A.-S., F.G., U.B., and J.O.R. analyzed and interpreted the data. C.A.-S., S.L., F.G., and J.O.R. wrote the manuscript. J.J.M, R.S., C.B., and U.B. critically revised the manuscript.

ACKNOWLEDGMENTS

We thank Vytautas Gapsys for fruitful discussions and for providing us with the GROMACS version with the soft-core potentials and the PMX library for the free energy calculations.

This work was supported with seed funds from the Deutsche Forschungsgemeinschaft, to the research unit FOR 1543: “Shear Flow Regulation of Hemostasis—bridging the gap between Nanomechanics and Clinical presentation, SHENC” (to all authors), the BIOMS postdoctoral program of the Heidelberg University (to C.A.-S.), and the Klaus Tschira Foundation (to F.G.). We gratefully acknowledge all SHENC members. S.L. thanks Elite Network of Bavaria for support.

SUPPORTING CITATIONS

References (40–55) appear in the Supporting Material.

REFERENCES

1. Springer, T. A. 2014. von Willebrand factor, Jedi knight of the bloodstream. *Blood.* 124:1412–1425.
2. Furlan, M., R. Robles, and B. Lämmle. 1996. Partial purification and characterization of a protease from human plasma cleaving von Willebrand factor to fragments produced by in vivo proteolysis. *Blood.* 87:4223–4234.
3. Sadler, J. E. 2002. A new name in thrombosis, ADAMTS13. *Proc. Natl. Acad. Sci. USA.* 99:11552–11554.
4. Dent, J. A., S. D. Berkowitz, …, Z. M. Ruggeri. 1990. Identification of a cleavage site directing the immunochemical detection of molecular abnormalities in type IIA von Willebrand factor. *Proc. Natl. Acad. Sci. USA.* 87:6306–6310.
5. Zhang, X., K. Halvorsen, …, T. A. Springer. 2009. Mechanoenzymatic cleavage of the ultralarge vascular protein von Willebrand factor. *Science.* 324:1330–1334.
6. Gao, W., P. J. Anderson, …, J. E. Sadler. 2006. Exosite interactions contribute to tension-induced cleavage of von Willebrand factor by the antithrombotic ADAMTS13 metalloprotease. *Proc. Natl. Acad. Sci. USA.* 103:19099–19104.
7. Baldauf, C., R. Schneppenheim, …, F. Gräter. 2009. Shear-induced unfolding activates von Willebrand factor A2 domain for proteolysis. *J. Thromb. Haemost.* 7:2096–2105.
8. Lippok, S., M. Radtke, …, J. O. Rädler. 2016. Shear-induced unfolding and enzymatic cleavage of full-length VWF multimers. *Biophys. J.* 110:545–554.
9. Furlan, M., R. Robles, …, B. Lämmle. 1998. von Willebrand factor-cleaving protease in thrombotic thrombocytopenic purpura and the hemolytic-uremic syndrome. *N. Engl. J. Med.* 339:1578–1584.
10. Tsai, H. M., and E. C. Lian. 1998. Antibodies to von Willebrand factor-cleaving protease in acute thrombotic thrombocytopenic purpura. *N. Engl. J. Med.* 339:1585–1594.
11. Bianchi, V., R. Robles, …, B. Lämmle. 2002. Von Willebrand factor-cleaving protease (ADAMTS13) in thrombocytopenic disorders: a severely deficient activity is specific for thrombotic thrombocytopenic purpura. *Blood.* 100:710–713.
12. Sadler, J. E. 2008. Von Willebrand factor, ADAMTS13, and thrombotic thrombocytopenic purpura. *Blood.* 112:11–18.
13. Ginsburg, D., and J. E. Sadler. 1993. von Willebrand disease: a database of point mutations, insertions, and deletions. For the Consortium on von Willebrand Factor Mutations and Polymorphisms, and the Subcommittee on von Willebrand Factor of the Scientific and Standardization Committee of the International Society on Thrombosis and Haemostasis. *Thromb. Haemost.* 69:177–184.
14. Schneppenheim, R., and U. Budde. 2011. von Willebrand factor: the complex molecular genetics of a multidomain and multifunctional protein. *J. Thromb. Haemost.* 9 (*Suppl. 1*):209–215.
15. Zhang, Q., Y.-F. Zhou, …, T. A. Springer. 2009. Structural specializations of A2, a force-sensing domain in the ultralarge vascular protein von Willebrand factor. *Proc. Natl. Acad. Sci. USA.* 106:9226–9231.
16. Interlandi, G., M. Ling, …, W. E. Thomas. 2012. Structural basis of type 2A von Willebrand disease investigated by molecular dynamics simulations and experiments. *PLoS One.* 7:e45207.
17. Hassenpflug, W. A., U. Budde, …, R. Schneppenheim. 2006. Impact of mutations in the von Willebrand factor A2 domain on ADAMTS13-dependent proteolysis. *Blood.* 107:2339–2345.
18. Lippok, S., T. Obser, …, J. O. Rädler. 2013. Exponential size distribution of von Willebrand factor. *Biophys. J.* 105:1208–1216.
19. Schneppenheim, R., H. Plendl, and U. Budde. 1988. Luminography—an alternative assay for detection of von Willebrand factor multimers. *Thromb. Haemost.* 60:133–136.
20. Budde, U., R. Schneppenheim, …, I. Peake. 2008. Detailed von Willebrand factor multimer analysis in patients with von Willebrand disease in the European study, molecular and clinical markers for the diagnosis and management of type 1 von Willebrand disease (MCMDM-1VWD). *J. Thromb. Haemost.* 6:762–771.
21. Elson, E. L., and D. Magde. 1974. Fluorescence correlation spectroscopy. I. Conceptual basis and theory. *Biopolymers.* 13:1–27.
22. Kato, S., M. Matsumoto, …, Y. Fujimura. 2006. Novel monoclonal antibody-based enzyme immunoassay for determining plasma levels of ADAMTS13 activity. *Transfusion.* 46:1444–1452.
23. Zanardelli, S., A. C. Chion, …, D. A. Lane. 2009. A novel binding site for ADAMTS13 constitutively exposed on the surface of globular VWF. *Blood.* 114:2819–2828.
24. Crooks, G. 1998. Nonequilibrium measurements of free energy differences for microscopically reversible Markovian systems. *J. Stat. Phys.* 90:1481–1487.

25. Shirts, M. R., E. Bair, …, V. S. Pande. 2003. Equilibrium free energies from nonequilibrium measurements using maximum-likelihood methods. *Phys. Rev. Lett.* 91:140601.
26. Goette, M., and H. Grubmüller. 2009. Accuracy and convergence of free energy differences calculated from nonequilibrium switching processes. *J. Comput. Chem.* 30:447–456.
27. Seeliger, D., and B. L. de Groot. 2010. Protein thermostability calculations using alchemical free energy simulations. *Biophys. J.* 98:2309–2316.
28. Van Der Spoel, D., E. Lindahl, …, H. J. C. Berendsen. 2005. GROMACS: fast, flexible, and free. *J. Comput. Chem.* 26:1701–1718.
29. Hess, B., C. Kutzner, …, E. Lindahl. 2008. GROMACS 4: algorithms for highly efficient, load-balanced, and scalable molecular simulation. *J. Chem. Theory Comput.* 4:435–447.
30. Pronk, S., S. Páll, …, E. Lindahl. 2013. GROMACS 4.5: a high-throughput and highly parallel open source molecular simulation toolkit. *Bioinformatics.* 29:845–854.
31. Grässle, S., V. Huck, …, S. W. Schneider. 2014. von Willebrand factor directly interacts with DNA from neutrophil extracellular traps. *Arterioscler. Thromb. Vasc. Biol.* 34:1382–1389.
32. Schrödinger, LLC. 2010. The PyMOL Molecular Graphics System, Version 1.3r1.
33. Krivobokova, T., R. Briones, …, B. L. de Groot. 2012. Partial least-squares functional mode analysis: application to the membrane proteins AQP1, Aqy1, and CLC-ec1. *Biophys. J.* 103:786–796.
34. Costescu, B. I., and F. Gräter. 2013. Time-resolved force distribution analysis. *BMC Biophys.* 6:5.
35. Jin, M., S. Cataland, …, H. M. Wu. 2006. A rapid test for the diagnosis of thrombotic thrombocytopenic purpura using surface enhanced laser desorption/ionization time-of-flight (SELDI-TOF)-mass spectrometry. *J. Thromb. Haemost.* 4:333–338.
36. Jin, M., T. C. Casper, …, H. M. Wu. 2008. Relationship between ADAMTS13 activity in clinical remission and the risk of TTP relapse. *Br. J. Haematol.* 141:651–658.
37. Singh, I., E. Themistou, …, S. Neelamegham. 2009. Fluid shear induces conformation change in human blood protein von Willebrand factor in solution. *Biophys. J.* 96:2313–2320.
38. Dehouck, Y., J. M. Kwasigroch, …, M. Rooman. 2011. PoPMuSiC 2.1: a web server for the estimation of protein stability changes upon mutation and sequence optimality. *BMC Bioinformatics.* 12:151.
39. Gapsys, V., S. Michielssens, …, B. L. de Groot. 2016. Accurate and rigorous prediction of the changes in protein free energies in a large-scale mutation scan. *Angew. Chem. Int. Ed. Engl.* 55:7364–7368.
40. Kirkwood, J. G. 1935. Statistical mechanics of fluid mixtures. *J. Chem. Phys.* 3:300–312.
41. Parrinello, M., and A. Rahman. 1981. Polymorphic transitions in single crystals: a new molecular dynamics method. *J. Appl. Phys.* 52:7182–7190.
42. Jorgensen, W. L., J. Chandrasekhar, …, M. L. Klein. 1983. Comparison of simple potential functions for simulating liquid water. *J. Chem. Phys.* 79:926–935.
43. Berendsen, H. J. C., J. P. M. Postma, …, J. R. Haak. 1984. Molecular dynamics with coupling to an external bath. *J. Chem. Phys.* 81:3684–3690.
44. Miyamoto, S., and P. A. Kollman. 1992. Settle: an analytical version of the SHAKE and RATTLE algorithm for rigid water models. *J. Comput. Chem.* 13:952–962.
45. Darden, T., D. York, and L. Pedersen. 1993. Particle mesh Ewald: An $N \log(N)$ method for Ewald sums in large systems. *J. Chem. Phys.* 98:10089–10092.
46. Essmann, U., L. Perera, …, L. G. Pedersen. 1995. A smooth particle mesh Ewald method. *J. Chem. Phys.* 103:8577–8593.
47. Hess, B., H. Bekker, …, J. G. E. M. Fraaije. 1997. LINCS: a linear constraint solver for molecular simulations. *J. Comput. Chem.* 18:1463–1472.
48. Feenstra, K. A., B. Hess, and H. J. C. Berendsen. 1999. Improving efficiency of large time-scale molecular dynamics simulations of hydrogen-rich systems. *J. Comput. Chem.* 20:786–798.
49. Hornak, V., R. Abel, …, C. Simmerling. 2006. Comparison of multiple Amber force fields and development of improved protein backbone parameters. *Proteins.* 65:712–725.
50. Bussi, G., D. Donadio, and M. Parrinello. 2007. Canonical sampling through velocity rescaling. *J. Chem. Phys.* 126:014101.
51. Joung, I. S., and T. E. Cheatham, 3rd. 2008. Determination of alkali and halide monovalent ion parameters for use in explicitly solvated biomolecular simulations. *J. Phys. Chem. B.* 112:9020–9041.
52. Best, R. B., and G. Hummer. 2009. Optimized molecular dynamics force fields applied to the helix-coil transition of polypeptides. *J. Phys. Chem. B.* 113:9004–9015.
53. Lindorff-Larsen, K., S. Piana, …, D. E. Shaw. 2010. Improved side-chain torsion potentials for the Amber ff99SB protein force field. *Proteins.* 78:1950–1958.
54. Gapsys, V., D. Seeliger, and B. L. de Groot. 2012. New soft-core potential function for molecular dynamics based alchemical free energy calculations. *J. Chem. Theory Comput.* 8:2373–2382.
55. Gapsys, V., S. Michielssens, …, B. L. de Groot. 2015. pmx: automated protein structure and topology generation for alchemical perturbations. *J. Comput. Chem.* 36:348–354.

Biophysical Journal, Volume *112*

Supplemental Information

Mutation G1629E Increases von Willebrand Factor Cleavage via a Cooperative Destabilization Mechanism

Camilo Aponte-Santamaría, Svenja Lippok, Judith J. Mittag, Tobias Obser, Reinhard Schneppenheim, Carsten Baldauf, Frauke Gräter, Ulrich Budde, and Joachim O. Rädler

Supporting material for

Mutation G1629E Increases von Willebrand Factor Cleavage via a Cooperative Destabilization Mechanism

C. Aponte-Santamaría, S. Lippok, J.J. Mittag, T. Obser, R. Schneppenheim, C. Baldauf, F. Gräter, U. Budde, and J.O. Rädler

S1. Diffusion constant of recombinant VWF constructs

We observed that cleavage rates were increased for cleavage of rVWF-G1629E compared to cleavage of denatured rVWF-wt. We assumed that the denaturing buffer only partly opens the rVWF-wt molecule, while the mutation might induce a more pronounced conformational change. This assumption is in line with a study of Singh *et al.* who showed that urea-containing buffer only partly destabilizes VWF and does not completely open the A2 cleavage domain (1). To quantify the difference in dimer conformation as a result of urea-containing buffer with the impact of the G1629E mutation on its conformation, we compared the diffusion coefficients of rVWF-wt dimer in nondenaturing and denaturing buffer, and rVWF-G1629E dimer (Figure S1). We obtained an extremely small difference for the diffusion constants of the various scenarios: $D_{wt,nd} = 20.2\,\mu\mathrm{m}^2/\mathrm{s}$ (nondenaturing conditions), $D_{wt,d} = 19.5\,\mu\mathrm{m}^2/\mathrm{s}$ (denaturing conditions, (2)), and $D_{G1629E,nd} = 18.9\,\mu\mathrm{m}^2/\mathrm{s}$ (nondenaturing conditions). These data confirm the conception of only partly opening due to urea, while the mutation induces an increased destabilization.

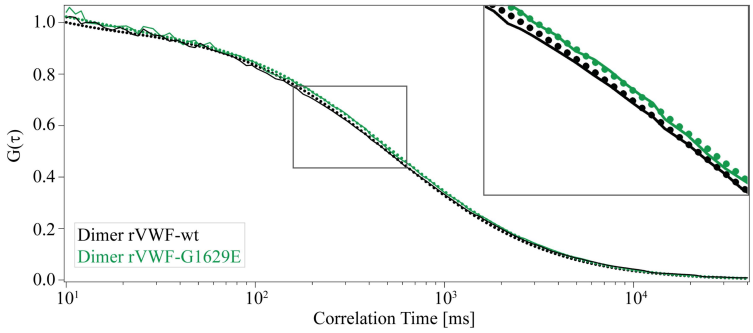

Figure S1. Autocorrelation curves of rVWF-wt dimer and rVWF-G1629E dimer under nondenaturing conditions. Change in diffusion constant reflects the conformational change of the rVWF dimer due to mutation G1629E. The diffusion coefficient of rVWF-wt dimer under denaturing conditions has been published before (2). Inset: Magnification to illustrate the change in the diffusion constant.

S2. Free energy calculations

Free energy differences were obtained by thermodynamic integration (3), gradually morphing the glycine residue into a glutamic acid (Figure S2A). The Hamiltonian of the system, H, was coupled to a parameter λ:

$$H = H_{gly}\lambda + H_{glu}(1-\lambda). \tag{1}$$

Thus, at $\lambda = 1$ it corresponded to the Hamiltonian of the glycine residue, while at $\lambda = 0$ to the one of the glutamic acid. The work associated to such morphing transitions was computed by

$$w_{G\to E} = \int \frac{\partial H}{\partial \lambda} d\lambda. \tag{2}$$

From the "forward" ($P_{G\to E}(w)$) and the "reverse" work distribution ($P_{E\to G}(w)$), the free energy ΔF was obtained, through the Crooks fluctuation theorem (4):

$$\frac{P_{G\to E}(w)}{P_{E\to G}(-w)} = \exp\left[\beta(w - \Delta F)\right]. \tag{3}$$

Here $\beta = 1/\left(k_B T\right)$, with k_B the Boltzmann constant, and T the temperature. ΔF was computed from the non-equilibrium work values, by means of the Bennett acceptance ratio as a maximum likelihood estimator (here called BAR-ML), a method proposed by Shirts *et al.* (5) to derive equilibrium free energies from non-equilibrium transitions. Assuming equal number of forward and reverse transitions, the maximum-likelihood estimate reads (5, 6)

$$\left\langle \frac{1}{1+\exp\left[\beta(w-\Delta F)\right]} \right\rangle_{G\to E} = \left\langle \frac{1}{1+\exp\left[-\beta(w-\Delta F)\right]} \right\rangle_{E\to G}, \tag{4}$$

where $\langle\rangle$ denotes average over transitions. ΔF was obtained by solving numerically equation 4, as proposed earlier in (6, 7) by using the "analyze_crooks" script from the pmx library (8, 9).

Uncertainty of ΔF was estimated by bootstrapping, solving equation 4, 100 times, by randomly selecting different forward and reverse work data sets in each run. This bootstrap calculation was also performed with the help of the the "analyze_crooks" script (8, 9).

For comparison, a rough estimate of the free energy was obtained, as the work value w^* at which the two distributions intersected: $P_{G\to E}(w^*) = P_{E\to G}(-w^*)$ and thereby $\Delta F = w^*$ (Intercept, figure S2B,C, right). Work distributions were generated reducing the bin size (Figure S2B,C, insets). The free energy was found in the bin where the two distributions overlapped. The bin size at which the free energy stabilized around a constant value (changes smaller than 0.5 %) was considered (the middle as the free energy estimate and half its size as an upper boundary of the free energy uncertainty). For $\Delta F1$ and $\Delta F2$, a bin size of 9 kJ/mol (thus an upper boundary of the uncertainty of 4.5 kJ/mol) was obtained.

400 free energy runs were performed for each transition (Figure S2B,C, left panels). For the transition in the folded state, the residue G1629 of the VWF A2 domain was morphed to obtain $\Delta F1$. Instead, for the transition in the unfolded state, the middle glycine of a GGG tri-residue peptide (which resembles a totally stretched fragment) was morphed to obtain $\Delta F2$. Errors obtained separately for $\Delta F1$ and $\Delta F2$, were propagated to obtain the error of $\Delta F1 - \Delta F2$. In addition, a static estimate of $\Delta F1 - \Delta F2$ was obtained from the PoPMuSIC web server (10) based on the X-ray structure of the A2 domain.

S3 Molecular dynamics simulations parameters and algorithms

Molecular dynamics (MD) simulations were carried out with the GROMACS package (11–13), equilibrium runs with the 4.5.5 version and non-equilibrium free energy transitions with the 4.6 version.

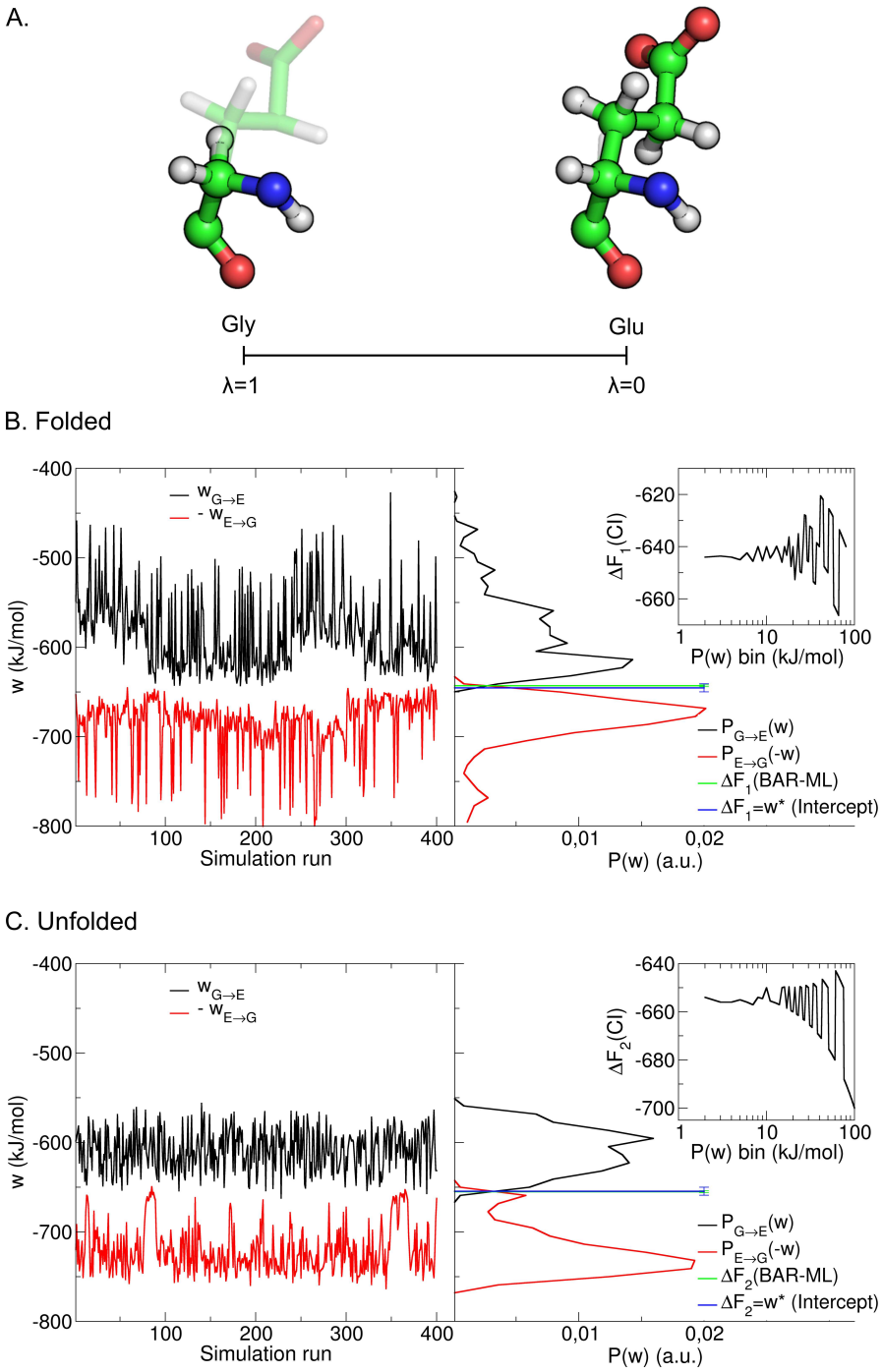

Figure S2. Free energy calculations to investigate the thermodynamic stability of the A2 domain upon G1629E mutation. A. Morphing of a glycine residue into a glutamic acid, by gradually varying an external coupling parameter λ from 1 to 0. **B, C.** Work and free energies obtained from multiple non-equilibrium MD transitions in the folded (B) and the unfolded (C) state. In the folded state, the G1629 residue of the VWF A2 domain was morphed. In the unfolded state, the middle glycine of a tri-residue GGG peptide was morphed. (Left) Work extracted from the glycine to glutamic acid transition (black) and minus the work of its reverse transition (red) (N=400). (Right) Work distributions for the indicated transitions (black and red). Free energy estimated with the Bennett acceptance ratio as a maximum-likelihood estimator (BAR-ML) is highlighted in green. Rough estimate from the work value w^* at which the two distributions intercept is depicted with the blue line (Intercept). (Right-inset) Free energy (estimated as the interception point) as a function of the bin size of the distributions. For a bin size smaller than 9 kJ/mol, the free energy estimate stabilized around a constant value (This was the value shown with the blue line). The free energy estimates were -643.0(2.0) kJ/mol for $\Delta F1$ (folded state) and -654.8(1.3) kJ/mol for $\Delta F2$ (unfolded state), using BAR-ML. A rough estimate from the intercept yielded -645.4(4.5) kJ/mol for $\Delta F1$ and -654.5(4.5) kJ/mol for $\Delta F2$. Values in parentheses are the error estimates which are upper boundaries in the case of the Intercept method. $\Delta F2 - \Delta F1$ are the values presented in Figure 4 of the main text.

Equilibrium MD simulations

The Amber99sb-ildn* force field (14–16), the TIP3P model (17), and Joung parameters (18) were used for the protein, the water molecules, and the ions, respectively. Non-bonded short-range interactions were considered by a Lennard-Jones potential within a cut-off region of 1 nm. Electrostatic interactions were computed by using the particle-mesh Ewald method (19, 20). The LINCS (21) algorithm together with virtual interaction-sites (22) were included to constraint all the bonds lengths and angular motions involving hydrogen atoms inside the protein. The SETTLE algorithm (23) was used to constraint both bond lengths and angles for the water molecules. Constraints algorithms allowed to numerically integrate Newtonian equations of motion at discrete time steps of 4 fs by using the leap frog algorithm. Temperature was held constant by coupling the system to a velocity-rescaling thermostat (24, 25) (reference temperature=300 K and coupling constant $\tau = 0.5$ ps). Pressure was maintained constant by using the Parrinello-Rahman barostat (26) (reference pressure=1 bar and coupling constant $\tau = 5.0$ ps). Production runs were preceded by a steepest-decent energy minimization and 1-ns solvent equilibration steps, with the protein harmonically restrained (harmonic force constant of 1000 kJmol^{-1}nm^{-2}) in the latter.

Non-equilibrium free-energy MD simulations

Each transition was conducted during 400 ps of non-equilibrium MD. Starting conformations were selected from the equilibrium MD simulations of the wt VWF A2 domain (for forward transition), G1629E VWF A2 mutant (for reverse transition), and from 50 ns equilibrium MD simulations of the GGG and GEG peptides for the forward and reverse transition, respectively. Same simulation parameters were used as for the equilibrium MD simulations of the VWF A2 domain, except that no restriction on the angular degrees of freedom of hydrogens were imposed, thus implying a time step of 2 fs. Also, an additional 500 ps solvent equilibration step (with the protein harmonically fixed, elastic constant of 1000 kJmol^{-1}nm^{-2}) preceded all the free energy runs of the A2 domain. An additional sodium ion, changing its charge from $q = 1$ ($\lambda = 0$) to $q = 0$ ($\lambda = 1$), was added to compensate for the appearance of the glutamic acid charge, and thereby the system was maintained electrically neutral. Soft-core potential functions (27) were used for the non-bonded interactions (α=0.3, σ=0.25, and a soft-core power of 1). The GROMACS version including soft-core potential functions was kindly provided by Vytautas Gapsys.

S4. Partial least squares functional mode analysis

A partial least squares functional mode analysis (PLS-FMA) (28) was carried out to identify structural changes induced by the G1629E mutation. The PLS-FMA method is a multivariate linear regression of the form $f(t) = X(t)B + E$, in which the time-dependent functional variable $f(t)$ is maximally correlated with the time-dependent atom positions $X(t)$ of a set of atoms. This is done through the collective vector B, by minimizing the square roots of the E residuals. Displacements along the collective vector B (called PLS vector) are correlated with changes in $f(t)$. B is constructed as a linear combination of uncorrelated k regressors (PLS components), each one constructed from a linear combination of the original coordinates $X(t)$ which maximizes the covariance with $f(t)$.

In our case the functional variable f was the mutation state of the A2 domain, ranging between zero (wild type) to one (G1629E). We thus assigned the number zero to all snapshots of the wild type trajectories and one to the ones of the G1629E trajectories (Black line in Figure S3A). $X(t)$ were the time-dependent atomic coordinates of the backbone and first carbon of the side chains of the A2 domain, extracted from the simulations. The PLS vector B separates the structures associated with wild type from the ones associated the G1629E mutant. The first part of the wild type A2 domain, and G1629E mutant MD trajectories (in the time window between 50 ns to 125 ns of each run) were concatenated to calculate B (light gray in Figure S3A). The remaining part (time windows between 125 ns and the end of the simulations) were used a posteriori to validate the resulting B (dark gray in Figure S3A). By considering few PLS components (k) a high correlation (>0.8) was obtained in the validation data set (Figure S3B), thus validating the used approach. Structural differences presented in the main text correspond to the extreme structures separated by B, obtained as a linear combination of 4 PLS components (correlation of 0.95).

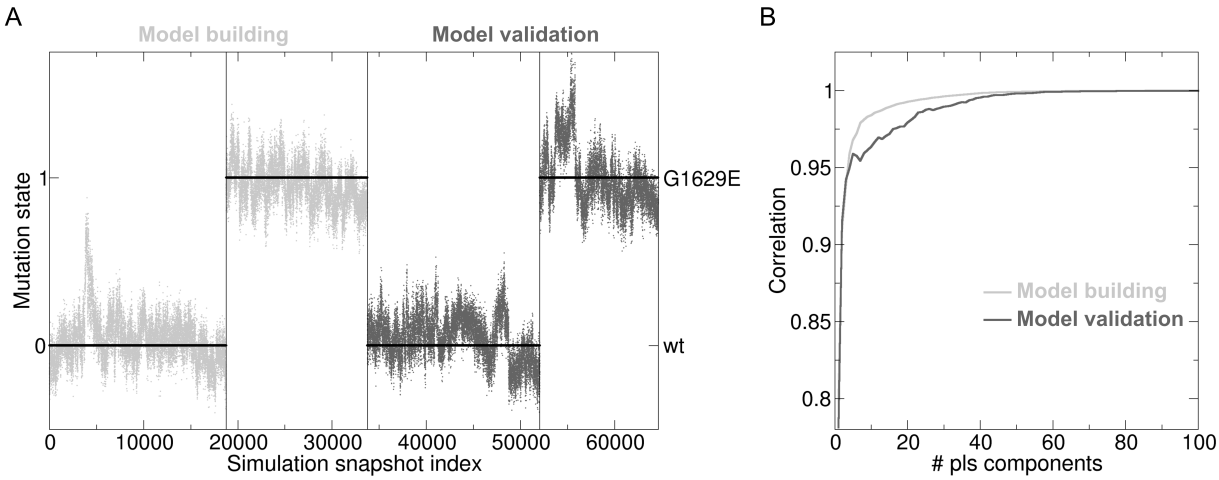

Figure S3. Partial least square functional mode analysis (PLS-FMA) to identify conformational changes due to the G1629E mutation during MD simulations of the VWF A2 domain. A. More than 60.000 snapshots were extracted from the MD trajectories of the A2 domain (both in its wild type or mutated form). Snapshots were labeled according to their mutation state: "0" if they corresponded to the wt or "1" to G1629E domain trajectories (see mutation state in black). Trajectories were splitted in two time windows: from 50 ns to 125 ns and from 125 ns to the end of the simulation. The first parts (50 ns-125 ns) were concatenated (both wt and mutant), to build the PLS vector (model building part). The second parts (>125 ns) were also concatenated and used to validate the resulting PLS vector (model validation part). From the obtained PLS vector, the mutation state was predicted , both for the model (light gray) and validation (dark gray) parts. **B.** The PLS vector was constructed by increasing the number of indepentent PLS components, and the correlation to the mutation state was monitored, both in the model building (light gray) and validation (dark gray) parts. In A, prediction of the mutation state was done with 4 PLS components.

Supporting material references

[1] Singh, I. T., P. Efrosyni, L. Porcar, and S. Neelamegham, 2009 Fluid shear induces conformation change in human blood protein von Willebrand factor in solution. *Biophys J* 96:2313–2320.

[2] Lippok, S., T. Obser, J. P. Müller, V. K. Stierle, M. Benoit, U. Budde, R. Schneppenheim, and J. O. Rädler, 2013. Exponential size distribution of von Willebrand factor. *Biophys J* 105:1208–1216.

[3] Kirkwood, J. G., 1935. Statistical mechanics of fluid mixtures. *The Journal of Chemical Physics* 3:300–313.

[4] Crooks, G., 1998. Nonequilibrium measurements of free energy differences for microscopically reversible Markovian systems. *Journal of Statistical Physics* 90:1481–1487.

[5] Shirts, M. R., E. Bair, G. Hooker, and V. S. Pande, 2003. Equilibrium free energies from nonequilibrium measurements using maximum-likelihood methods. *Phys Rev Lett* 91:140601.

[6] Goette, M., and H. Grubmüller, 2009. Accuracy and convergence of free energy differences calculated from nonequilibrium switching processes. *J Comput Chem* 30:447–456.

[7] Gapsys, V., S. Michielssens, D. Seeliger, and B. L. de Groot, 2016. Accurate and rigorous prediction of the changes in protein free energies in a large-scale mutation scan. *Angew Chem Int Ed Engl* 55:7364–7368.

[8] Seeliger, D., and B. L. de Groot, 2010. Protein thermostability calculations using alchemical free energy simulations. *Biophys J* 98:2309–2316.

[9] Gapsys, V., S. Michielssens, D. Seeliger, and B. L. de Groot, 2015. pmx: Automated protein structure and topology generation for alchemical perturbations. *Journal of computational chemistry* 36:348–354.

[10] Dehouck, Y., J. M. Kwasigroch, D. Gilis, and M. Rooman, 2011. PoPMuSiC 2.1: a web server for the estimation of protein stability changes upon mutation and sequence optimality. *BMC Bioinformatics* 12:151.

[11] Spoel, D. V. D., E. Lindahl, B. Hess, G. Groenhof, A. E. Mark, and H. J. C. Berendsen, 2005. GROMACS: fast, flexible, and free. *J Comput Chem* 26:1701–1718.

[12] Hess, B., C. Kutzner, D. van der Spoel, and E. Lindahl, 2008. GROMACS 4: Algorithms for highly efficient, load-balanced, and scalable molecular simulation. *J Chem Theory Comput* 4:435–447.

[13] Pronk, S., S. Pll, R. Schulz, P. Larsson, P. Bjelkmar, R. Apostolov, M. R. Shirts, J. C. Smith, P. M. Kasson, D. van der Spoel, B. Hess, and E. Lindahl, 2013. GROMACS 4.5: a high-throughput and highly parallel open source molecular simulation toolkit. *Bioinformatics* 29:845–854.

[14] Hornak, V., R. Abel, A. Okur, B. Strockbine, A. Roitberg, and C. Simmerling, 2006. Comparison of multiple Amber force fields and development of improved protein backbone parameters. *Proteins: Struct Funct Bioinf* 65:712–725.

[15] Best, R. B., and G. Hummer, 2009. Optimized molecular dynamics force fields applied to the helix-coil transition of polypeptides. *J Chem Phys B* 113:9004–9015.

[16] Lindorff-Larsen, K., S. Piana, K. Palmo, P. Maragakis, J. L. Klepeis, R. O. Dror, and D. E. Shaw, 2010. Improved side-chain torsion potentials for the Amber ff99SB protein force field. *Proteins: Struct Funct Bioinf* 78:1950–1958.

[17] Jorgensen, W. L., J. Chandrasekhar, J. D. Madura, R. W. Impey, and M. L. Klein, 1983. Comparison of simple potential functions for simulating liquid water. *J Chem Phys* 79:926–935.

[18] Joung, I. S., and T. E. Cheatham, 2008. Determination of alkali and halide monovalent ion parameters for use in explicitly solvated biomolecular simulations. *J Chem Phys B* 112:9020–9041.

[19] Darden, T., D. York, and L. Pedersen, 1993. Particle mesh Ewald: An Nlog(N) method for Ewald sums in large systems. *J Chem Phys* 98:10089–10092.

[20] Essmann, U., L. Perera, M. L. Berkowitz, T. Darden, H. Lee, and L. G. Pedersen, 1995. A smooth particle mesh Ewald method. *J Chem Phys* 103:8577–8593.

[21] Hess, B., H. Bekker, H. J. C. Berendsen, and J. G. E. M. Fraaije, 1997. LINCS: A linear constraint solver for molecular simulations. *J Comput Chem* 18:1463–1472.

[22] Feenstra, K. A., B. Hess, and H. J. C. Berendsen, 1999. Improving efficiency of large time-scale molecular dynamics simulations of hydrogen-rich systems. *J Comput Chem* 20:786–798.

[23] Miyamoto, S., and P. A. Kollman, 1992. Settle: An analytical version of the SHAKE and RATTLE algorithm for rigid water models. *J Comput Chem* 13:952–962.

[24] Berendsen, H. J. C., J. P. M. Postma, W. F. van Gunsteren, A. DiNola, and J. R. Haak, 1984. Molecular dynamics with coupling to an external bath. *J Chem Phys* 81:3684–3690.

[25] Bussi, G., D. Donadio, and M. Parrinello, 2007. Canonical sampling through velocity rescaling. *J Chem Phys* 126:014101 – 014101–7.

[26] Parrinello, M., and A. Rahman, 1981. Polymorphic transitions in single crystals: A new molecular dynamics method. *J Appl Phys* 52:7182–7190.

[27] Gapsys, V., D. Seeliger, and B. L. de Groot, 2012. New soft-core potential function for molecular dynamics based alchemical free energy calculations. *Journal of Chemical Theory and Computation* 8:2373–2382.

[28] Krivobokova, T., R. Briones, J. S. Hub, A. Munk, and B. L. de Groot, 2012. Partial least-squares functional mode analysis: application to the membrane proteins AQP1, Aqy1, and CLC-ec1. *Biophys J* 103:786–796.